Stochastic Environmental Research and Risk Assessment (2022) 36:373–388
https://doi.org/10.1007/s00477-021-02138-2

ORIGINAL PAPER

# Land subsidence prediction using recurrent neural networks

**Sunil Kumar**[1] · **Dheeraj Kumar**[1] · **Praveen Kumar Donta**[2] · **Tarachand Amgoth**[2]

Accepted: 10 November 2021 / Published online: 24 November 2021

## Abstract

In an environment, one of the natural geological hazards is land surface subsidence. Underground mining and subsurface coal fires are primarily responsible for subsidence of land. Activities, such as, over-exploitation of coal, minerals, groundwater and petroleum resources, depillaring of the existing galleries and water logging of the relinquished galleries are the major factors resulting in subsidence. The deformation is primarily measured in terms of change in ground elevation values (Z-dimension) at different time intervals at identified ground locations. All the conventional and exiting techniques have certain limitations in monitoring and predicting land surface subsidence. In this work, we predict the land subsidence in Jharia Coalfield, Dhanbad, India for one year in the interval of twelve days on the datasets collected through a monitoring technique called Modified PSInSAR. The sample datasets contains 14 locations and 67 previous land subsidence value calculated from each location. We train and test predictive models and perform the prediction of the land subsidence using Vanilla and Stacked long short-term memories. Finally, we demonstrate the predicted deformation values of the 14 locations for one year. The prediction model shows the subsidence rate in Nai-dunia basti near Jharia, Dhanbad is alarming as 93.8 mm/year where as Digwadih and Godhar showed the critical rate as 82 mm/year.

**Keywords** Deformation monitoring · Land subsidence prediction · Modified PSInSAR · Recurrent neural networks · Vanilla and stacked LSTM

## 1 Introduction

In an environment, one of the natural geological hazards is land surface subsidence. Underground mining and subsurface coal fires are primarily responsible for subsidence of land. Activities, such as, over-exploitation of coal, minerals, groundwater and petroleum resources, depillaring of the existing galleries and water logging of the relinquished galleries are the major factors resulting in subsidence (Kumar et al. 2020; Pandey et al. 2016; Chatterjee 2006; Jianjun et al. 2012). Subsidence vulnerability becomes more in those areas where large underground voids have been created by extracting coals, ores, etc. (Ishwar and Kumar 2017; Qin and Perissin 2015; Engelbrecht and Inggs 2013; Paradella et al. 2015; Gupta et al. 2014; Guang et al. 2009; Miao et al. 2008). It is very terrible as it involves human loss and great loss of national properties. It also affects the surface and subsurface water resources and the ultimate result is the degradation of the environment. Mine subsidence can take a shape of disaster in inhabited areas if preventive measures are not taken in time. Unfortunately, the increasing demand of energy and mineral resources worldwide has brought mechanization and rapid expansion of mining activities. With the increase of mining activities, there will be a corresponding increase in mine subsidence problems causing more damage unless proper subsidence control measures are taken. Control measures are directly dependent on detection, monitoring and prediction pattern of subsidence area. Spatial-temporal monitoring and need for precise calculation of land subsidence for mapping in zonal management and corresponding control of surface

---

✉ Tarachand Amgoth
tarachand@iitism.ac.in

Sunil Kumar
skumar781@iitism.ac.in

Dheeraj Kumar
dheeraj@iitism.ac.in

[1] Department of Mining Engineering, Indian Institute of Technology (Indian School of Mines), Dhanbad, Jharkhand 826004, India

[2] Department of Computer Science and Engineering, Indian Institute of Technology (Indian School of Mines), Dhanbad, Jharkhand, India

deformation caused by both underground mining and subsurface fires. However, the effectiveness of the preventative and protective measures of subsidence greatly depends upon the accuracy of subsidence monitoring and associated prediction parameters.

Most of the existing techniques of subsidence monitoring are based on ground-level that rely on the instruments as Precise Level (PL), Auto Level (AL), Digital Level (DL), Total Station (TS), etc. These instruments with associated field survey techniques provide a highly relevant measurement with a millimeter accuracy, but very cumbersome in comparison to modern geo-spatial techniques. Ground-based subsidence monitoring methods are also not safe because measurements are required to be taken along subsidence prone areas. Global Navigation Satellite System (GNSS) based techniques have made the measurement quite easier in terms of portability of the instruments and satellite dependencies for the data acquisition (Chatterjee et al. 2015; Wang et al. 2011; Jing-Xiang and Hong 2009; Lü et al. 2008). However, GNSS suffers from some of the same vexing problems as physical movement required in subsidence prone areas with very costly instruments. The limitations of GNSS techniques have been overcome by spaceborne imaging techniques. Spaceborne subsidence monitoring has emerged as a better technique after the development of Synthetic Aperture Radar (SAR) Interferometry. The radar satellites can observe almost anywhere on the surface with ease, even during darkness and cloudy conditions, which makes it invaluable for subsidence monitoring. Interferometric Synthetic Aperture Radar (InSAR) technique uses two or more SAR images to generate maps of surface deformation or digital elevation, using differences in the phase of the waves returning to the satellites. Its limitation is accuracy as atmospheric errors introduce several errors. When images are acquired at different times (temporal baseline), utilizing the Differential SAR Interferometry (DInSAR) technique, it is possible to measure the changes of the surface elevation. These measurements are shown by a series of colored bands, the so-called fringes or interferogram as shown in Fig. 1, as the Angarpathra, Godhar, and Bastacola mines of Jharia coal field (JCF).[1] The DInSAR technique also has limitations of accuracy and reliability of specific area deformation. The Persistent Scatterer Interferometric Synthetic Aperture Radar (PSInSAR) technique shows relatively better results for deformation of the land surface and with higher accuracy.

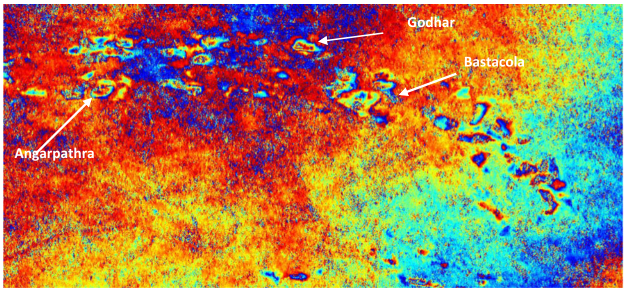

**Fig. 1** Fringes by DInSAR processed of ALOS PALSAR Images in mines of JCF

The Long short-term memory (LSTMs) are the variants of recurrent neural networks (RNNs) mainly used for time series forecasting. The LSTMs are categorized into Vanilla, Bidirectional, and Stacked LSTMs. The LSTMs have been used to predict the Land subsidence in (Li et al. 2020; Qiao et al. 2020; Mubashar et al. 2021; Pu et al. 2018) and Bidirectional LSTMs are used in (Shen et al. 2021; Qu et al. 2019). The LSTMs are efficiently predicting the Land subsidence from the given datasets with better accuracy. It is better to use the Bidirectional LSTMs because it processes the data in both forward and backward time order. The Vanilla and Stacked LSTMs are the variants of LSTMs, where Vanilla LSTMs reduces the memory usage four times better than the LSTMs. So that we can minimize the additional memories during evaluation, and it also speeds up the training and testing. The stacked LSTMs are performing the operations simultaneously using a hierarchy of hidden layers, and it evaluates the complex data very easily with improved accuracy (Gangopadhyay et al. 2018; Liang et al. 2018).

Our research is based on the processing and analysis of free available SAR datasets as SENTINEL-1A SAR data. These SAR Datasets are available on a specific web portal in archive format for the researchers' but lagging by a few months to be available some times. The modified PSInSAR technique is giving large Excel sheet of movement of location termed as PS point and pictorial view with coded colour to identify subsidence on map. The Vertical movement of the PSs near GNSS control stations (Fig. 2) have been validated with processed GNSS data output. Here an excel sheet of 26,000 rows and 100 columns had been generated but we ran a sample of 14 rows data sets to study the LSTM module for 1-year prediction. The prediction is for the future so the output of the processed SAR data in Excel format is transferred to the LSTM module for further prediction at 12 days' intervals for a year. This prediction is giving alarming information to deal with settlement and inhabitants residing in the vicinity and saving the life and economy of the nation.

The contributions of this article are summarized as follows:

- We develop a modified PSInSAR processing Technique by changing the range, subset area, pixel value, boxcut

---

[1] Jharia coal field (JCF), Jharkhand state, India.

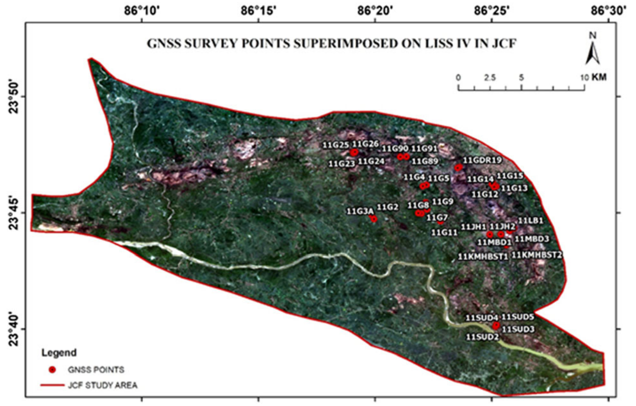

**Fig. 2** Shows the GNSS survey points superimposed on LISS IV in Jharia Coal field, India

filtering on SAR images. This processing technique helps in increasing the accuracy of the deformation velocity. The outcome of the approach is in the form of colour coded subsidence locations, referred as Permanent Scatterers (PSs). In our experiment, we considered SAR images of Sentinel-1A of JCF and converted them into PSs

- The movement of PSs are validated with the processed GNSS Data. This strategy helps in assessment of accuracy of deformation obtained by modified PSInSAR. After validation, the PSs of higher coherence are selected for model testing and converted into numerical format and stored in excel using SAR data processing tool called SARPROZ.
- The excel sheet consists of 26,000 rows and 100 columns generated using SARPROZ tool and we use a sample of 14 rows datasets to predict the land subsidence using LSTM.
- Train and test the data for accurate predictions of the land surface subsidence using Vanilla and Stacked LSTMs.
- We present the comparisons of observed and predicted values of land subsidence in JCF of mining as well as GNSS-based locations. Finally we also present the predicted values of land surface subsidence for one year.
- All the predicted locations are finally validated with physical site visits accordingly. The prediction showed the subsidence rate in Nai-dunia basti in JCF is alarming as 93.8 mm /year whereas Digwadih and Godhar showed the critical rate as 82 mm/year.

The remaining sections of this article is arranged as follows. In Sect. 2, we review some of the existing but related approaches for land subsidence prediction in Mining areas. In Sect. 3, we provide the preliminaries used in the problem formulation. In Sect. 4, we describe the proposed model in detail. In Sect. 5, we present the experimental results of the proposed algorithm. This paper is concluded in Sect. 6.

## 2 Related work

In recent years Jharia Coal field (JCF) has witnessed large number of land subsidence and coal fires. Underground activities and coal fires are main cause of such incidents. Nearly 150 such cases have been reported in the past decade. In (BCCL 2008), Master plan prepared by Bharat Coking Coal Limited (BCCL) in association with central mine planning and design institute (CMPDI) also signifies huge losses in BCCL due to mine fire and induced subsidence in rural as well as urban area of JCF.

The researchers have used conventional DInSAR techniques for monitoring long-term land subsidence phenomenon and achieved the deformation by analyzing the fringes obtained by SAR images (Chatterjee et al. 2006; Strozzi et al. 2001; Lanari et al. 2004; Raucoules et al. 2003; Amelung et al. 2000). However, the conventional DInSAR techniques have limitations in terms of (1) very small spatial baseline ($<200$ m) (2) baseline dependent accuracy of external DEM (3) no reduction of atmospheric phase. To overcome the limitations associated with conventional DInSAR techniques, a first-generation time series InSAR (Advanced DInSAR) technique was introduced by (Ferretti et al. 2001). Many researchers have worked on advanced DInSAR techniques and developed different approaches to deformation analysis (Hooper et al. 2004; Hooper and Zebker 2007; Hooper 2008; Crosetto et al. 2005; Mora et al. 2003; Schmidt and Bürgmann 2003). Many studies have been taken out internationally for land subsidence monitoring using Advance DInSAR techniques (Dong et al. 2013; Qin and Perissin 2015; Chatterjee et al. 2015, 2016; Ishwar and Kumar 2017; Engelbrecht et al. 2011; Gupta et al. 2014; Przyłucka et al. 2015).

In order to overcome the limitations of second generation advanced DInSAR techniques, the development of the Persistent Scatterer Interferometric Synthetic Aperture Radar (PSInSAR) technique took place to detect land deformation at the millimeter level. The PSInSAR technique is the geodetic SAR processing technique that uses two or more SAR images to generate maps of topography or deformation of the Earth’s surface (Prati et al. 2010; Hooper et al. 2012; Mura et al. 2016).

The PSInSAR technique has been applied in the coal filed or nearby areas to detect land deformation using C-Band and L-Band SAR Data (Abdikan et al. 2014; Thapa et al. 2016). The short wavelength C-band is more suitable to detect slow velocity subsidence if the optimal baseline is maintained, whereas long wavelength L-band can effectively detect rapid velocity subsidence (Chatterjee et al. 2015; Abdikan et al. 2011; Yue et al. 2011). Its limitation is as less number of PSs achieved due to exclusion of partially correlated scatterers for the analysis resulting in some information losses in the vicinity.

The authors in (Perissin and Wang 2011) have developed a modified PSInSAR approach which is also called Persistent Scatterer Interferometry (PSI). In PSI the correlated scatterers are also included along with permanent scatterers to increase the point target density in the highly susceptible area for decorrelation (Sefercik and Soergel 2014). PSI is more reasonable than the Advance DInSAR time series for recognizing most stable scattered pixels where pixel properties don't fluctuate with time and radar look point (Crosetto et al. 2016; Mura et al. 2016).

A study conducted by Central Ground Water Board (CGWB), in Lucknow city, indicated land subsidence is likely to occur due to over exploitation of groundwater in the next 15–20 years if immediate step to increase recharge is not taken at some of the localities of Lucknow in Uttar Pradesh: such as Narhi, Charbagh, Rajajipuram and Gomtinagar regions may see land subsidence by 2026 (Trivedi 2020).

The authors in (Zhou et al. 2017) have studied the spatial–temporal analysis of land subsidence caused by groundwater pumping from 2010 to 2015 in the Beijing plain using the SBAS InSAR technique. 69 interferograms generated using 47 TerraSAR images were utilized to investigate the land subsidence where long haul groundwater over exploitation and the use of shallow metropolitan space has prompted land subsidence. The highest yearly land subsidence rate was 146 mm/year from 2011 to 2015. The study between the SBAS InSAR results and the ground leveling measurements demonstrated that the SBAS InSAR results accomplished an accuracy of 2 mm. This research work is aimed at the study of the feasibility of the modified PSInSAR technique with C-band SAR data for finding the slow surface deformation caused by coal mine fire and underground mining activities in JCF. Also, a multi-temporal analysis of SAR images of ENVISAT ASAR has been carried out for monitoring and mapping of temporal land subsidence of the area under study. The modified PSI technique has proven its ability to detect land subsidence over the vegetated and rural areas. It also resolves low spatial density of permanent scatterers by considering partially correlated scatterers as permanent scatterers (PSs) and extracting information from these PSs. The study has been focused on detecting continuous slow rate subsidence of fifteen major sites of JCF. The imaging techniques also reduce the safety risk and decrease the expenses that are inherent in conventional methods due to extensive fieldwork. In this study, the SAR images acquired by SENTINEL-1A of the European Space agency have been processed by SARPROZ Software for deformation analysis of JCF, Dhanbad, India. Further Prediction analysis has been carried out for the determination of vertical shifting of the objects which will be helpful to the safe planning of the projects. In (Iwanec et al. 2016; sar 2019), authors have performed theoretical studies how to predict the subsidence above the single and multi-seam longwall mines. However, the work has certain limitations and the prediction is totally based on the physical conditions.

## 3 Preliminaries

In this section, we provide the preliminaries used in the proposed work. Long Short-Term Memory (LSTM) is used to time series forecasting (TSF). LSTM model that is used for univariate TSF problem is Univarite LSTM. While predicting the future values using the past observations through single series of observations and a model is a complicated issue.

As per earlier discussions, the LSTMs operate on sequential data and increasing the number of layers increases the levels of abstraction overtime on the input data. The network depth is more important than the number of memory cells considered for a layer. The LSTM with multiple layers is treated as Stacked LSTM. These upstream layers always provide the sequential output instead of a single output value. Each layer in Stacked LSTMs consider a 3D input for its memory cell and produce a single value as 2D array in an output. Each layer of the stacked LSTM is a chain-like processing framework shown in Fig. 3. The cell state in the Fig. 3 is running on top with minor interactions to just flow unchanged data. This layer can remove or add information to the cell state using the two gates such as $\otimes$ and $\oplus$. The $\sigma$ layer provide the values between 0 or 1 and it is described in Eq. (1).

$$\sigma = \begin{cases} 0 & \text{Nothing through} \\ 1 & \text{Everything through} \end{cases} \tag{1}$$

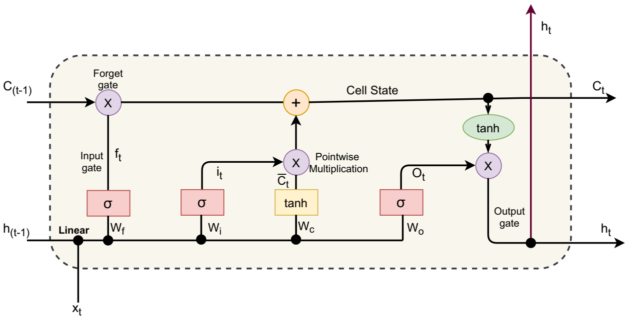

**Fig. 3** Structure of a LSTM

$$C_{(t-1)} = \begin{cases} 0 & \text{Get rid of complete data} \\ 1 & \text{Keep data completely} \end{cases} \tag{2}$$

The process framework performs mainly four operations to produce the final outcome. First, the forget gate starts removing the useless informations form the input gate as shown in Eq. 3. It provides input data to the sigmoid function ($\sigma(\ldots)$) such as previous layer output i.e. $h_{t-1}$ and hidden layers feature information $x_t$. The $f_t$ maps the previous layer cell state output i.e. $C_{t-1}$ to the current cell state $C_t$.

$$f_t = \sigma\left(W_f[h_{t-1}, x_t] + b_f\right) \tag{3}$$

where $W_f$ is the weight matrix and $b_f$ is the bias vector of the forget gate. The $\sigma$ is computed as shown in Eq. (4).

$$\sigma(a) = \frac{1}{1 + e^{-a}} \tag{4}$$

In the next state, the LSTM performs two operations $\sigma(\ldots)$ and $\tanh(\ldots)$ simultaneously to update the current cell state $C_t$ as shown in Eqs. (5, 6), respectively. The $\sigma(\ldots)$ and $\tanh(\ldots)$ produces the $i_t$ and $\overline{C}_t$, respectively using previous layer output i.e. $h_{t-1}$ and hidden layers feature information $x_t$.

$$i_t = \sigma(W_i[h_{t-1}, x_t] + b_i) \tag{5}$$

$$\overline{C}_t = \tanh(W_c[h_{t-1}, x_t] + b_c) \tag{6}$$

where $W_i$ and $W_c$ are the weight matrix of input gate and state update vector, respectively, and $b_i$ and $b_c$ are the bias vectors of input gate and state update vector, respectively. The hyperbolic tangent function is represented using tanh and it is computed as shown in Eq. (7).

$$tanh(a) = \frac{e^a - e^{-a}}{e^a + e^{-a}} \tag{7}$$

Finally, the current state of LSTM has been updated using previous two operations as shown in Eq. (8).

$$C_t = (C_{t-1} \otimes f_t) + \left(i_t \otimes \overline{C}_t\right) \tag{8}$$

where $\otimes$ is point-wise scalar multiplication of the vectors.

In the last phase, the LSTM produces the output through output gate by using the current cell state information. The outputs such as $O_t$ and $h_t$ are computed as shown in Eqs. (9) and (10).

$$O_t = \sigma(W_o[h_{t-1}, x_t] + b_o) \tag{9}$$

$$h_t = O_t \otimes \tanh(C_t) \tag{10}$$

In general, the LSTM is comprised of a hidden layer followed by an output layer. Depends on the types of TSF problem, several LSTM techniques are existed in the literature among Vanilla and Stacked LSTMs are more popular. In this work, we tested two univariate LSTM model such as (1) Vanilla LSTM and (2) Stacked LSTM.

### 3.1 Vanilla LSTM and stacked LSTM

While making the prediction through Vanilla LSTM, it uses an output layer and a single hidden LSTM layer. It supports the sequence data as an input. The LSTM model reads single time step in each time, unlike the Convolution neural networks (CNN) and the data represented in state format while learning the model.

The LSTM can extend with multiple hidden layer which makes the deeper model called stacked LSTM and which reflects the deep learning model. Increasing the number of layers in the LSTM will increase the prediction accuracy. But, increasing the too many layers also increase the complexity as well the computational time. The additional layers recombine the representations to provide the new combinations of the predictions with increased abstraction. Instead of giving importance to the memory cells of a layer, considering the depth of network is more important. An LSTM produces the two dimensional output by taking the three dimensional input to the system while performing the learning process. This issue can be addressed by taking the output of each LSTM layer at each time stamp and set the input data with a return $sequences = True$ argument. This allow us to have three dimensional output from hidden LSTM layer as input to the next. Here we build both Vanilla LSTM and Stacked LSTM for predicting the next one Year land subsidence and compared both model with their loss and accuracy. These four steps discussed earlier will repeated over multiple LSTM layers as shown in Fig. 4.

## 4 Proposed work

The proposed model is illustrated and depict using flow chart shown in Fig. 5, which is primarily partitioned into four parts including data collection (along with masking), data augmentation, Training and Evaluation models. Using Vanilla and Stacked LSTMs, predicting land surface subsidence values for one year.

### 4.1 Data collection

A network of fifty eight Global navigation satellite system (GNSS) survey points established in JCF to find the subsidence magnitude during 11 phases of the survey at quarterly intervals. The GNSS data which we have collected has been processed with respect to BASE Station data. The errors during post-processing have been

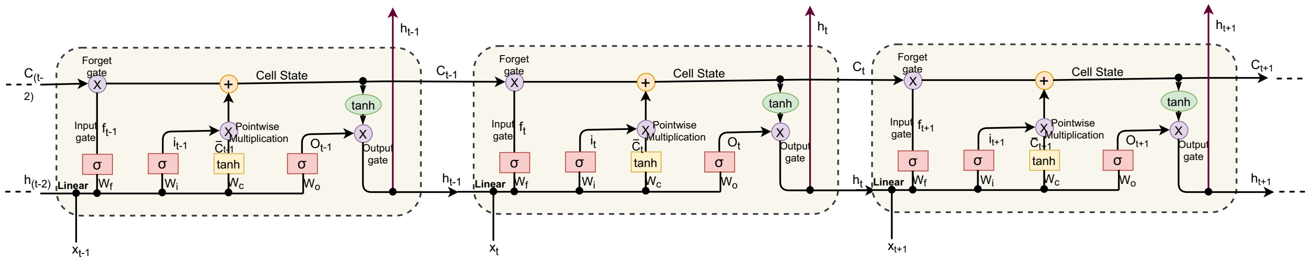

**Fig. 4** Structure of Stacked LSTM

**Fig. 5** Flow chart of the proposed model

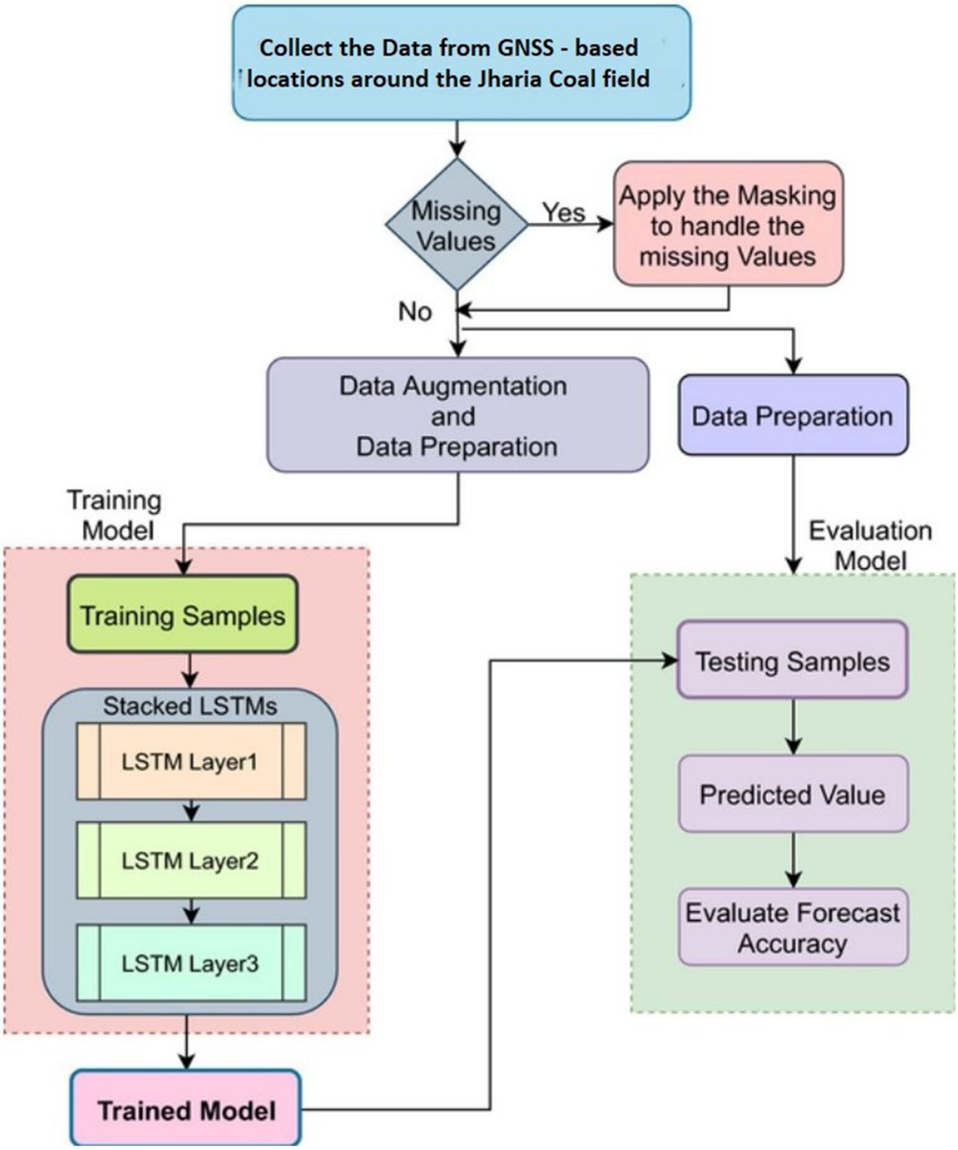

minimized by Precise Point Positioning. Archives data of the same time period has been made available by International GNSS Service (IGS) to reduce the ephemeris. Some important parameters are shown in Table 1 and locations are pointed on a map shown in Fig. 6. The measurement of land surface subsidence for some of the locations in JCF using GNSS are shown in Fig. 7. SAR images of SENTINEL-1A of the same period acquired from the European Satellite Agency. The 67 SAR Images of 12 days Temporal Resolution is processed in SARPROZ

**Table 1** Dataset locations

| Location ID | Latitude | Longitude | Altitude | Location | Displacement velocity (mm/year) | Cumulative displacement (mm) |
|---|---|---|---|---|---|---|
| L1 | 23.70349 | 86.42649 | 182.7 | East of barari masjid | − 72.6 | − 162.2 |
| L2 | 23.70618 | 86.42627 | 177.8 | Digwadih_NE | − 81.8 | − 182.7 |
| L3 | 23.70055 | 86.41453 | 162.5 | Didwadih | − 64.7 | − 144.5 |
| L4 | 23.73156 | 86.42495 | 184.6 | Nai dunia basti | − 93.8 | − 209.6 |
| L5 | 23.78219 | 86.39222 | 250.8 | Godhar near GDR19 | − 82 | − 183.3 |
| L6 | 23.73856 | 86.43497 | 210.3 | Laltenbasti | − 56.9 | − 127.1 |
| L7 | 23.74762 | 86.32791 | 203.5 | Garbhudi,Moonidih | − 27.2 | − 60.7 |
| L8 | 23.75829 | 86.37329 | 190.4 | Balihari,G21 | − 30 | − 67 |
| L9 | 23.75509 | 86.36283 | 239.6 | Aralgaria,G8 | − 26.8 | − 59.9 |
| L10 | 23.79083 | 86.35486 | 210.7 | Bansjora,G91 | − 27.8 | − 62 |
| L11 | 23.77601 | 86.42264 | 209 | Bastacola, nearG12 | − 30 | − 67 |
| L12 | 23.77514 | 86.38484 | 220.5 | Ghansadih Kendua | − 20.6 | − 46 |
| L13 | 23.77067 | 86.36826 | 216.8 | Gopalichak,G5 | − 25 | − 55.9 |
| L14 | 23.8002 | 86.43213 | 257.2 | Golf ground Dhanbad | 2.6 | 5.8 |

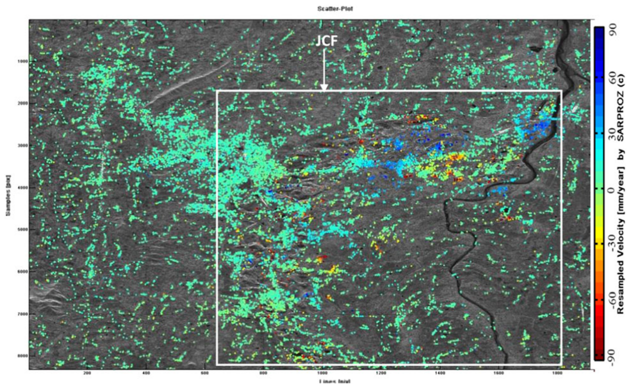

**Fig. 6** PSs in JCF generated by SARPROZ using processed 67 SAR images of SENTINEL-1A

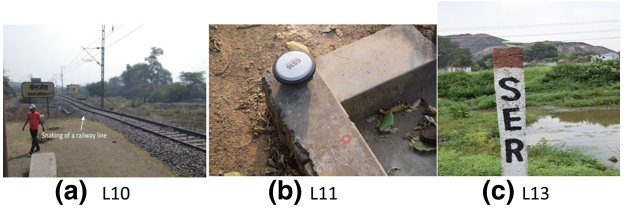

(a) L10 (b) L11 (c) L13

**Fig. 7** The GNSS survey points of locations L10, L11 and L13—

Software to obtain the persistent Scatterer in the JCF. During processing of SAR data by PSInSAR technique a huge excel sheet with a lot of information has been produced in terms of deformation magnitude of temporal baseline of SAR images coherence, Displacement velocity cumulative displacement etc. Ultimately the result of deformation will be up to the last date of the SAR image used. An excel sheet of 26,000 PSs obtained with more than 0.5 temporal coherence value after the processing. A sample of 22 locations has been collected covering a few of the GNSS survey points' locality of JCF. The GNSS processed result was used to validate the occurrence of subsidence shown by the PSInSAR technique. For further prediction the excel sheet of 14 locations is converted into Dataframe with normalized data (using pandas and sklearn python packages) which inputs the LSTM.

The JCF is a large coal mines area in India with 19.4 billion tonnes of available coal. Since 1916, this area suffered a coal bed fire and consumed nearly 37 millions tons of coal. It results in water and air pollution and also land subsidence in the cities of JCF (Pai and Carr-Wilson 2018). We consider various parameters from the JCF including the land type (Agricultural or Barren), transportation facility (Road, Rail, or others), Displacement velocity, depth of the seam and the SAR image availability from 03-10-2016 to 28-12-2018 on every twelve alternative days using the remote sensing. The land subsidence near to the river area is high as compared to the other areas during rainy seasons. In general, the land subsidence patterns have more diversity among the various locations around the Jharia coal field, and great challenges to predict the short-term land subsidence. The missing values during the data collection are masking based on the method used in (Che et al. 2018).

## 4.2 Data augmentation and preparation

For any machine learning methods including stacked LSTMs, training dataset is one of the important considerable factors. The best training dataset will be generated through data augmentation and preparation, and the process is summarized using Fig. 8. The primary goal of the data augmentation is to amplify training data by dividing

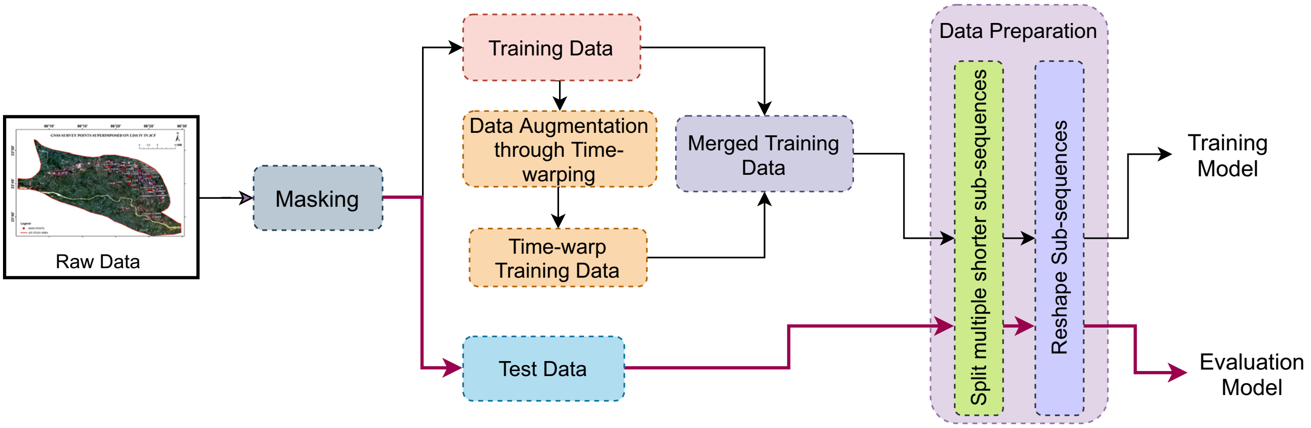

**Fig. 8** Process model of data augmentation and preparation

original data with overlaps to minimizes the complexity of the computations. In this work, we consider the time-warping data augmentation approach to prepare the data for training process. We operated with various warping ratios to show the variability of the synthetic training data (Rashid and Louis 2019). With this augmentation process, the training data increases 4-fold with various temporal length.

The data collected and augmented from the remote sensing is one dimensional, where the LSTM requires 3D input data. In data preparation phase, the data initially split in to multiple short sub-sequences and then reshape sub-sequences. We illustrate the data preparation through an example for better understand. The learning process of LSTMs follows a sequence of inputs to an output. *An Example of Univariate time series:* {6, 8, 10, 12, 13, 16, 18, 20, 22, 24, 26}. Split these series in to multiple input/output samples. Here, the input can contains more that one step (in this example we consider *three* and represented using $X$) and an output as one step (treated as $Y$) as shown below:

$$\begin{array}{cc} X & Y \\ [6\ 8\ 10] & 12 \\ [8\ 10\ 12] & 13 \\ [10\ 12\ 13] & 16 \\ \ldots & \ldots \\ [20\ 22\ 24] & 26 \end{array}$$

In this way, the input data split and reshare the data for providing the input to training or testing modules. The input data categorized into training and test data. The training data used in Stacked LSTM learning models where as the test data used for predicting the results.

**Table 2** Comparisons of Vanilla LSTM and Stacked LSTM Concerning $\mathcal{R}_m$ and $\mathcal{R}_p$

| Location | Vanilla LSTM | | Stacked LSTM | |
|---|---|---|---|---|
| | $\mathcal{R}_m$ | $\mathcal{R}_p$ | $\mathcal{R}_m$ | $\mathcal{R}_p$ |
| L1 | 0.0817 | 71.4 | 0.0139 | 88.204 |
| L2 | 0.062 | 74.96 | 0.038 | 80.364 |
| L3 | 0.059 | 75.68 | 0.050 | 77.639 |
| L4 | 0.053 | 76.85 | 0.0315 | 82.227 |
| L5 | 0.058 | 75.91 | 0.049 | 77.655 |
| L6 | 0.069 | 73.62 | 0.037 | 80.5 |
| L7 | 0.147 | 61.604 | 0.078 | 71.9 |
| L8 | 0.106 | 67.31 | 0.15 | 61.03 |
| L9 | 0.102 | 68.00 | 0.08 | 71.4 |
| L10 | 0.091 | 69.7 | 0.052 | 77.09 |
| L11 | 0.117 | 65.697 | 0.0512 | 77.35 |
| L12 | 0.067 | 74.01 | 0.047 | 78.28 |
| L13 | 0.055 | 76.46 | 0.0401 | 79.97 |
| L14 | 0.163 | 59.51 | 0.09 | 68.4 |

## 4.3 Training and evaluation model

The training data augmented and prepared for input to the Stacked LSTM. The over-fitting is avoided by adopting the dropout strategy after each LSTM for better generalization. The dropout rate is approximately 10% (Wei 2020). The stacked LSTM has the capability to handle the long and short-term time dependencies for forecasting the accurate land subsidence. The first LSTM layer sends a sequence vector to the next LSTM layer and so on. Each subsequent LSTM receives previous time stamp's feedback that either allow for process or drop the data. The basic working model of the stacked LSTM is presented in Sect. 3.

The test data prepared for testing only and no augmentation performed on it. After the model being learned, a

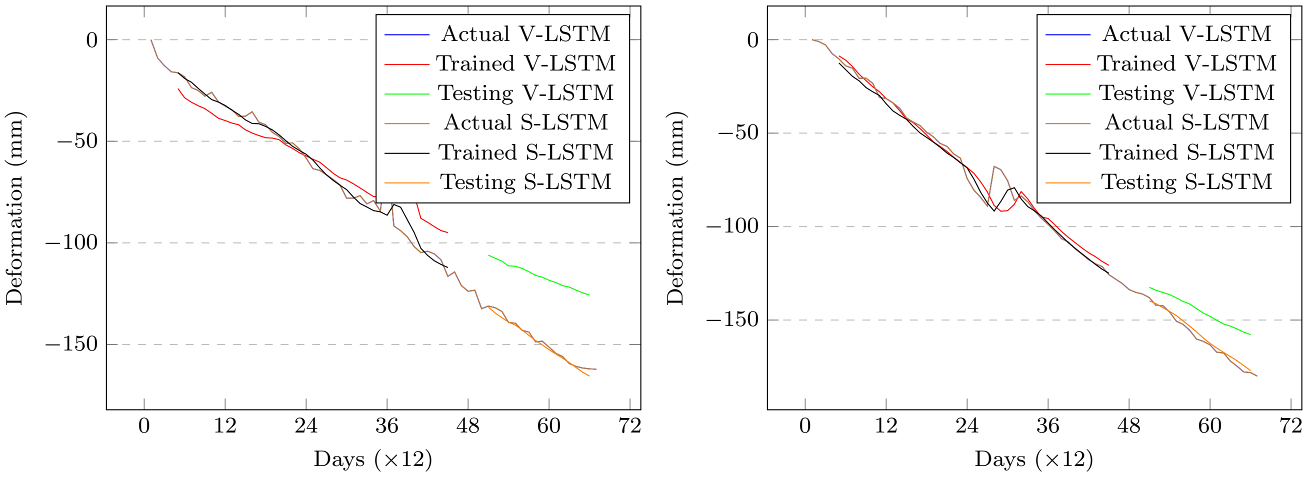

**(a)** L1 **(b)** L2

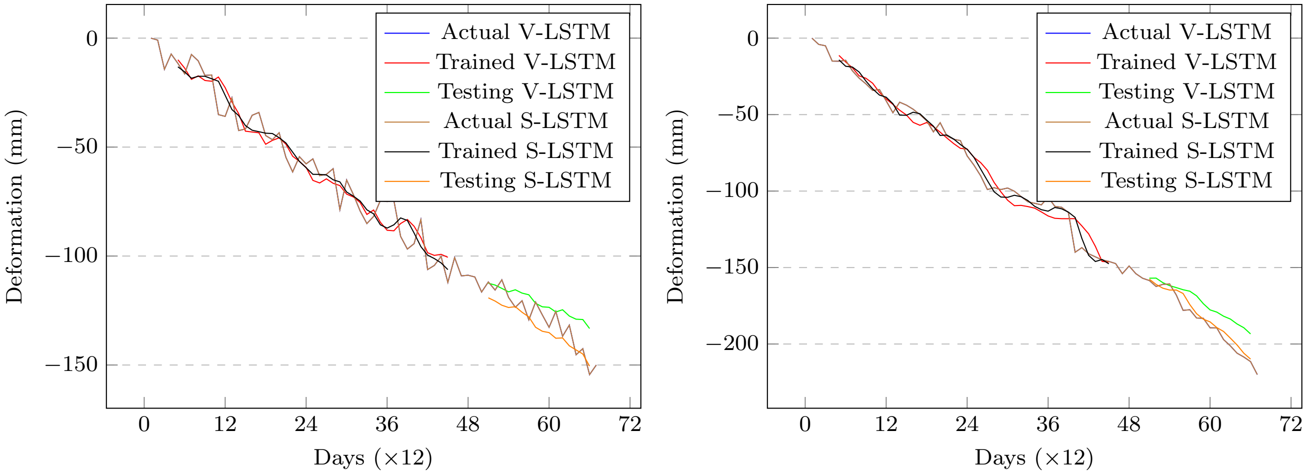

**(c)** L3 **(d)** L4

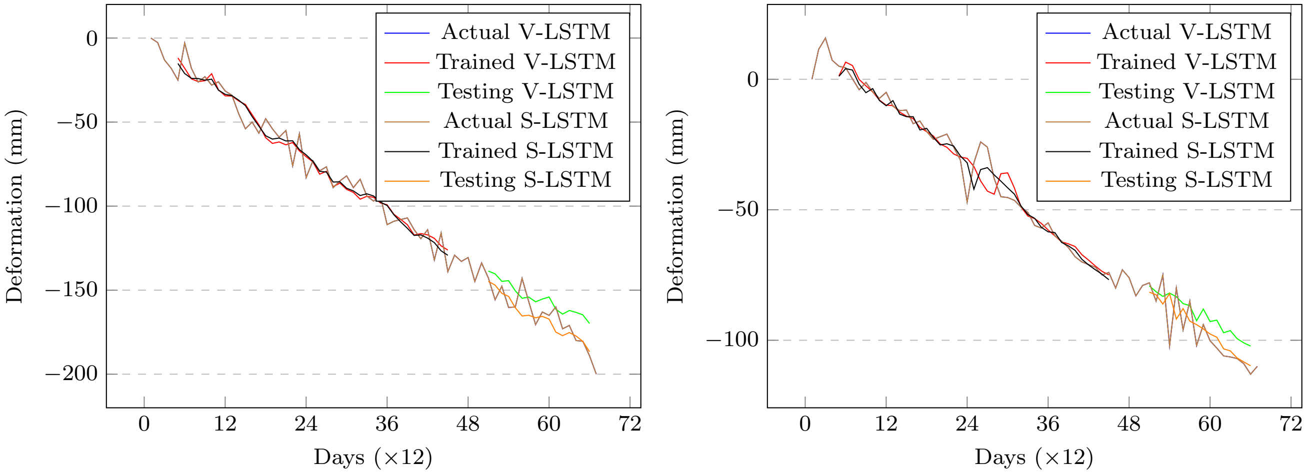

**(e)** L5 **(f)** L6

**Fig. 9** Comparison between the observed and predicted values of land subsidence of Location L1–L6 with Vanilla and Stacked LSTM model

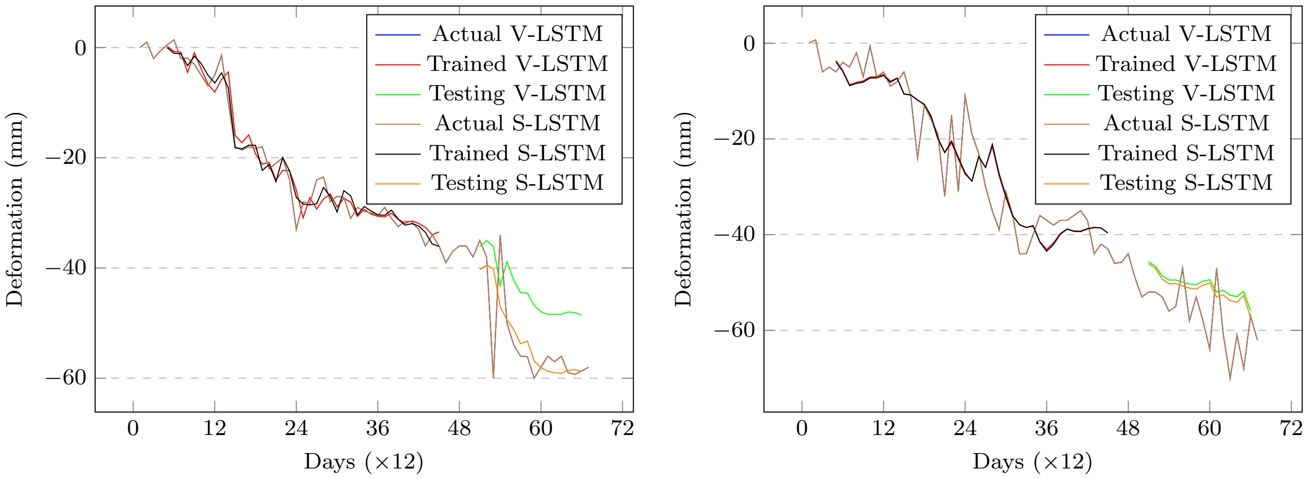

**(a)** L7 **(b)** L8

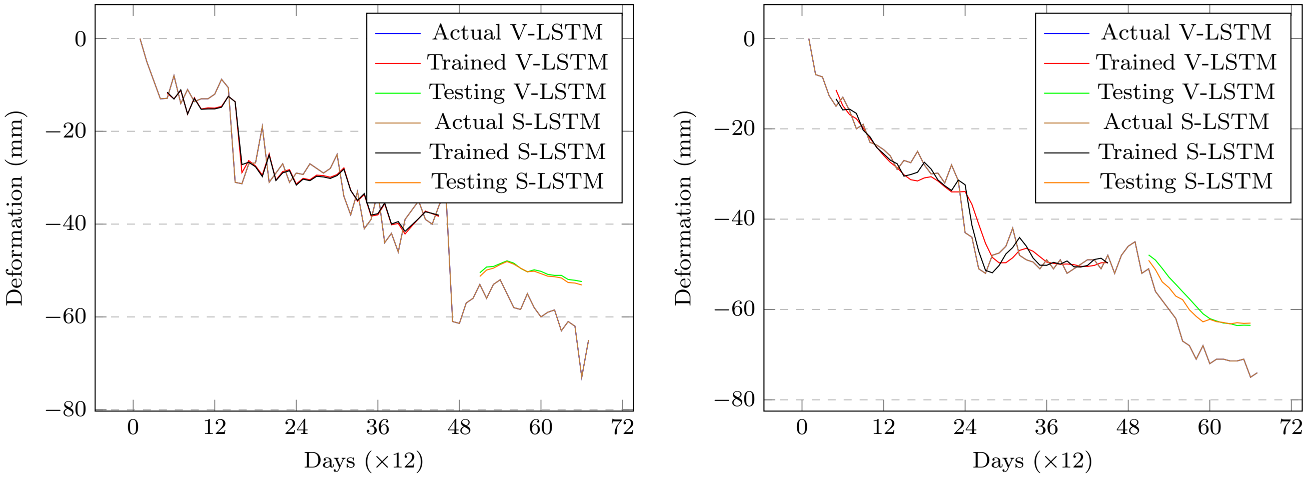

**(c)** L9 **(d)** L10

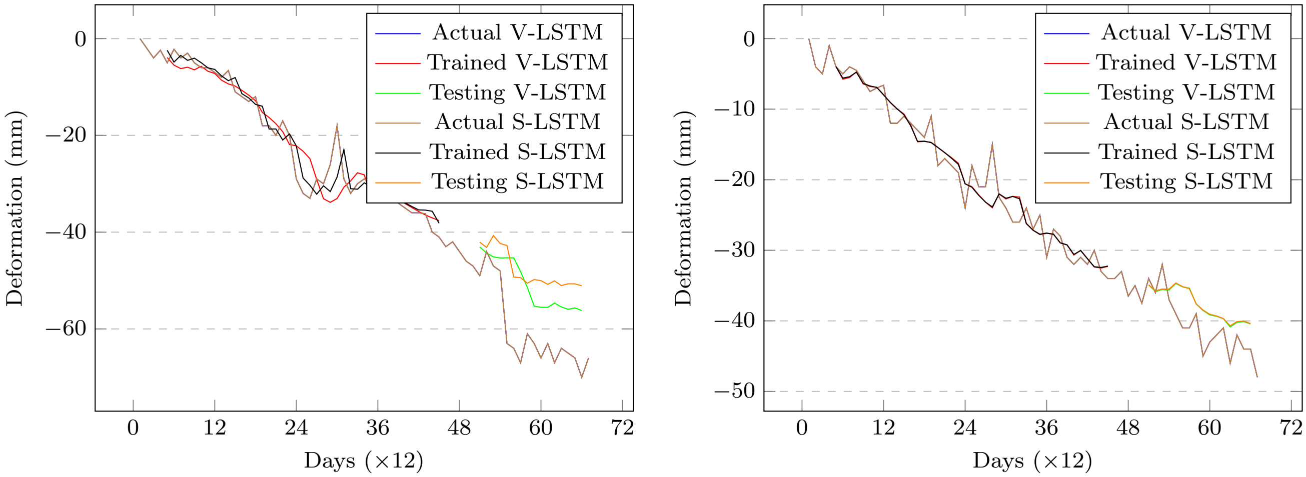

**(e)** L11 **(f)** L12

**Fig. 10** Comparison between the observed and predicted values of land subsidence of each Location L7–L12 with Vanilla and Stacked LSTMs model

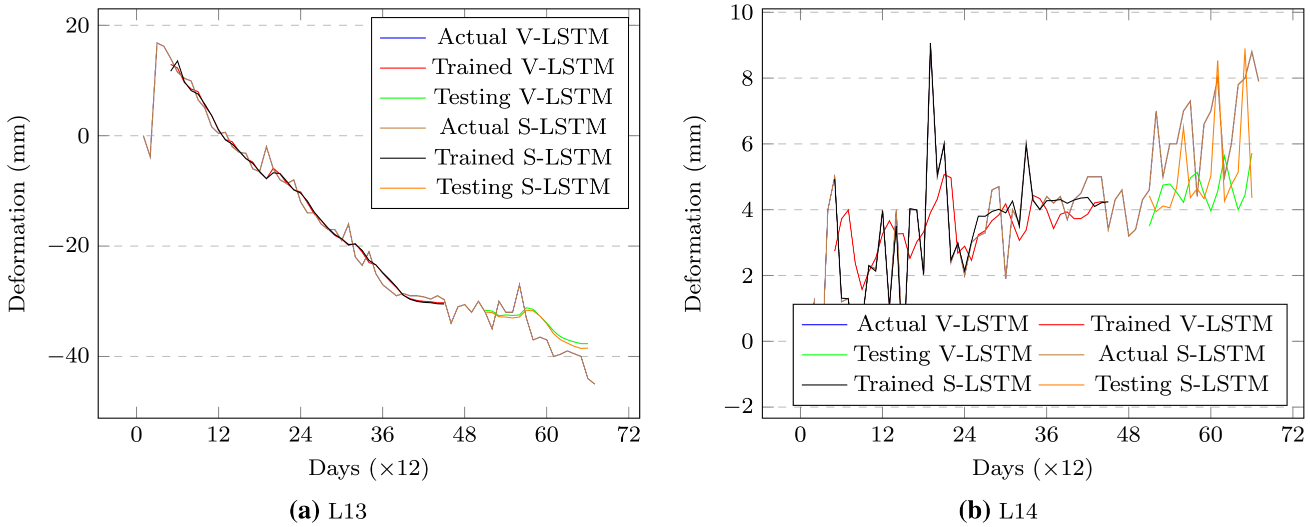

**(a)** L13 **(b)** L14

**Fig. 11** Comparison between the observed and predicted values of land subsidence of each Locations L13 and L14 with Vanilla and Stacked LSTMs model

test data set is taken as an input to evaluate the model efficiency and finally to validate the accuracy of the predicted values.

## 5 Experimental results

In this section we evaluate the prediction accuracy of the land subsidence through Vanilla LSTM and Stacked LSTM. Initially, we discuss the model construction followed by the results analysis.

### 5.1 Model construction

In this work, we collect the data from 14 locations around Jharia coal field from Jharkhand state in India between 3rd Oct 2016 to 28th Dec 2018, i.e. 817 days. We consider 14 environmental conditions and each condition 817 samples are collected. All these conditions are segmented with the length of 128 and 60% overlap. In this work, we use 64, 32, and 32 hidden units in LSTM layer 1, layer 2 and layer 3, respectively. The input layer has 128 units which is equal to input sample dimension. We can fit the training dataset once the complete model is defined. For the whole dataset, 70% is used for training and remaining used for testing. The Root Mean Square Error (RMSE) is an indicator to evaluate the performance of training model.

### 5.2 Results analysis

In this section, we compare the simulation results of Stacked LSTM and Vanilla LSTM using various metrics such as accuracy, land subsidence, and etc. The proposed approach used regression model, so Root mean squared error is a good measure of accuracy.

#### 5.2.1 Root mean square errors

It is measured as the difference between values predicted by a model and the values observed and it is denoted using $\mathcal{R}_m$. It is calculated using Eq. (11)

$$\mathcal{R}_m = \sqrt{\frac{\sum_{i=1}^{N}(X_i - \hat{X}_i)^2}{N}} \tag{11}$$

where $X_i$ is the actual data and $\hat{X}_i$ is the predicted data of data set $i$, and $N$ indicates the number of samples.

#### 5.2.2 Root mean absolute percentage errors

It is measured as the difference between values predicted by a model and the values observed and it is denoted as $\mathcal{R}_p$. It is calculated using Eq. (11)

$$\mathcal{R}_p = \frac{100}{\sqrt{N}} \times \sqrt{\sum_{i=1}^{N}\left(\frac{X_i - \hat{X}_i}{X_i}\right)^2} \tag{12}$$

where $X_i$ is the actual data and $\hat{X}_i$ is the predicted data of data set $i$, and $N$ indicates the number of samples. The comparison results of running example dataset in terms of $\mathcal{R}_m$ and $\mathcal{R}_p$ are presented in Table 2

The comparison between the observed and predicted train and test land subsistence (reduced level) values of Location L1–L14 with Vanilla LSTM and Stacked LSTM model are presented in Figs. 9, 10 and 11. We observe that the prediction accuracy of both the models is between 80%

**Table 3** Predicted Deformation values (mm) using Stacked LSTM

| Day (X 12) | L1 | L2 | L3 | L4 | L5 | L6 | L7 | L8 | L9 | L10 | L11 | L12 | L13 | L14 |
|---|---|---|---|---|---|---|---|---|---|---|---|---|---|---|
| 68 | − 165 | − 181 | − 150.1 | − 224 | − 202.4 | − 111 | − 59 | − 62.5 | − 66 | − 78 | − 68 | − 49 | − 48 | − 8 |
| 69 | − 172 | − 183.1 | − 164 | − 225 | − 212 | − 116 | − 60 | − 66 | − 70 | − 79 | − 70 | − 50 | − 54.2 | − 8.3 |
| 70 | − 175 | − 187 | − 157.2 | − 232 | − 218 | − 118 | − 59.6 | − 65 | − 83 | − 82 | − 70.2 | − 48 | − 52 | − 10 |
| 71 | − 176 | − 190 | − 161.3 | − 233 | − 224.1 | − 119 | − 59.5 | − 66.2 | − 82.2 | − 85.2 | − 75 | − 51 | − 51 | − 11 |
| 72 | − 178 | − 193.2 | − 166.1 | − 231 | − 227.2 | − 121 | − 61.4 | − 64 | − 78 | − 83 | − 72.5 | − 55 | − 53 | − 11.2 |
| 73 | − 201 | − 195 | − 157.8 | − 240.1 | − 229 | − 123 | − 62 | − 65 | − 84 | − 86 | − 74 | − 54 | − 58 | − 11.4 |
| 74 | − 202 | − 199 | − 160.3 | − 246.3 | − 238.2 | − 126 | − 61.8 | − 62 | − 81 | − 90.1 | − 73 | − 54.7 | − 55 | − 11 |
| 75 | − 204.5 | − 200.2 | − 167.2 | − 249 | − 236 | − 129 | − 63 | − 67 | − 83.8 | − 89 | − 75.1 | − 56 | − 56 | − 10.6 |
| 76 | − 205.7 | − 203 | − 166 | − 251 | − 240 | − 131.5 | − 64 | − 65 | − 84 | − 93 | − 76 | − 57.8 | − 58.1 | − 12 |
| 77 | − 207 | − 205 | − 180 | − 256 | − 238 | − 137.1 | − 67 | − 67 | − 85 | − 93.2 | − 76.6 | − 57 | − 59 | − 12.2 |
| 78 | − 209 | − 208 | − 181.1 | − 262 | − 241 | − 135.3 | − 65 | − 70 | − 84.6 | − 94 | − 77 | − 56 | − 60.4 | − 14 |
| 79 | − 211.4 | − 211.1 | − 175 | − 271 | − 245.2 | − 140.1 | − 61.8 | − 72 | − 90 | − 96 | − 78 | − 62 | − 60.6 | − 11 |
| 80 | − 214 | − 215 | − 185.2 | − 264 | − 251.1 | − 142.6 | − 69 | − 73 | − 91 | − 99.1 | − 80 | − 61 | − 62 | − 12.6 |
| 81 | − 214.5 | − 217 | − 181.1 | − 267 | − 263 | − 141 | − 75 | − 74 | − 101.7 | − 97 | − 81 | − 60 | − 63 | − 11 |
| 82 | − 212.5 | − 216 | − 177 | − 274.2 | − 255 | − 147.1 | − 78 | − 81 | − 102 | − 97.5 | − 82 | − 62.2 | − 63.2 | − 14 |
| 83 | − 217.3 | − 218 | − 176 | − 278 | − 265.5 | − 146 | − 78.2 | − 83 | − 108 | − 95 | − 84 | − 63 | − 66 | − 14.2 |
| 84 | − 218.1 | − 220 | − 189 | − 282 | − 259 | − 150.5 | − 78.1 | − 85 | − 105 | − 98 | − 82 | − 64 | − 66.5 | − 12 |
| 85 | − 221 | − 222.1 | − 191 | − 286 | − 264 | − 153.8 | − 78.5 | − 86 | − 115 | − 101 | − 88 | − 61 | − 62 | − 17 |
| 86 | − 223 | − 225 | − 188 | − 285 | − 268 | − 152 | − 82 | − 89 | − 130 | − 99.2 | − 90 | − 68 | − 66 | − 18 |
| 87 | − 224 | − 227.6 | − 199.2 | − 288 | − 270 | − 151.2 | − 81 | − 102 | − 129 | − 102 | − 91 | − 67 | − 68 | − 16 |
| 88 | − 223 | − 229 | − 201 | − 292 | − 273 | − 156 | − 80 | − 85 | − 127 | − 98.1 | − 97 | − 68 | − 68.5 | − 12 |
| 89 | − 226 | − 231 | − 203 | − 291 | − 278 | − 161 | − 84 | − 101 | − 131 | − 101.6 | − 100 | − 69 | − 68 | − 13 |
| 90 | − 229 | − 234 | − 207 | − 296 | − 289 | − 177 | − 83 | − 81 | − 129.2 | − 109 | − 109 | − 74 | − 72 | − 12.5 |
| 91 | − 232 | − 237 | − 205 | − 298 | − 285 | − 172 | − 78 | − 89 | − 130 | − 112 | − 112 | − 68 | − 73.2 | − 13.8 |
| 92 | − 233.6 | − 239 | − 213 | − 301 | − 290 | − 164 | − 78.3 | − 93 | − 127 | − 116 | − 113 | − 71 | − 74 | − 14.5 |
| 93 | − 225.4 | − 241 | − 212.1 | − 308 | − 295 | − 166 | − 74 | − 100 | − 128 | − 117 | − 112 | − 71 | − 76 | − 14.6 |
| 94 | − 227.2 | − 245 | − 209.8 | − 307 | − 296 | − 168.5 | − 73.1 | − 105 | − 131 | − 115 | − 115 | − 65 | − 76.4 | − 16.6 |

**Table 3** (continued)

| Day (X 12) | L1 | L2 | L3 | L4 | L5 | L6 | L7 | L8 | L9 | L10 | L11 | L12 | L13 | L14 |
|---|---|---|---|---|---|---|---|---|---|---|---|---|---|---|
| 95 | – 229 | – 245.3 | – 213 | – 315 | – 301.5 | – 169 | – 78 | – 109 | – 134.2 | – 114 | – 117 | – 72.2 | – 77 | – 16.9 |
| 96 | – 235 | – 248 | – 215 | – 317 | – 305 | – 172 | – 77 | – 101 | – 135 | – 118 | – 119 | – 74 | – 78 | – 17 |
| 97 | – 236 | – 251 | – 216 | – 318 | – 306.1 | – 173.1 | – 79 | – 106 | – 134.6 | – 120 | – 120 | – 76 | – 76 | – 19 |
| 98 | – 234 | – 252 | – 217 | – 321 | – 307 | – 174 | – 80.1 | – 114 | – 137 | – 120.1 | – 122 | – 79 | – 80 | 18.6 |

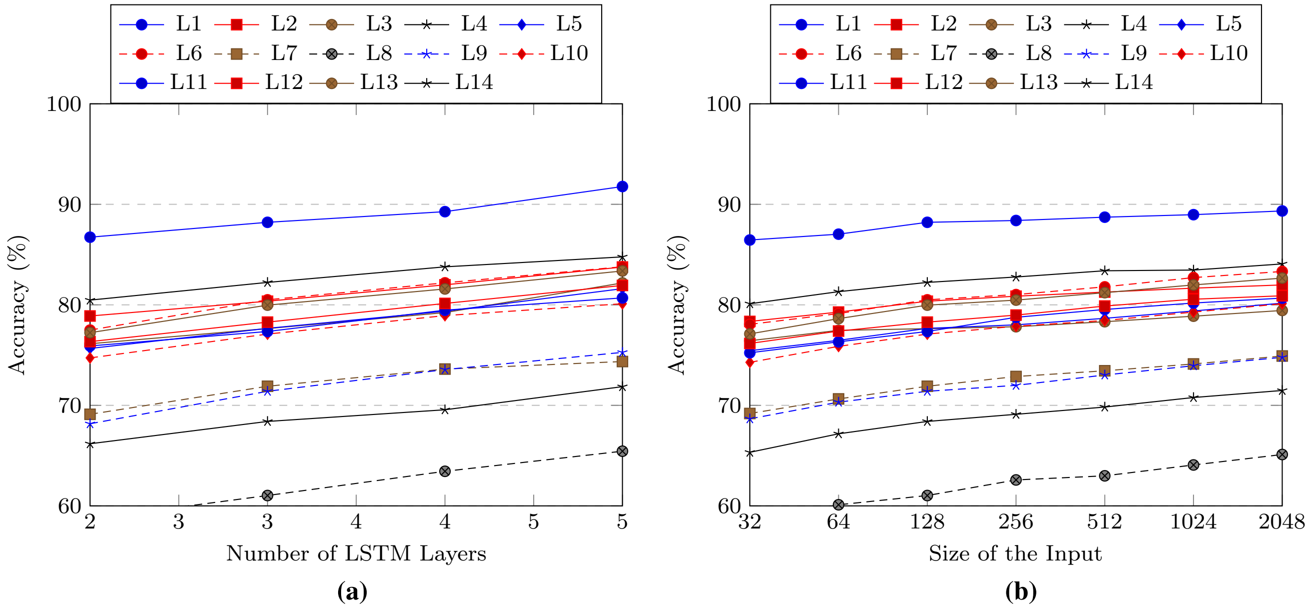

(a)

(b)

**Fig. 12** Influence of Accuracy with varying hyperparameters (**a**) #of LSTM Layers (**b**) size of input

to 95% for 14 locations. We estimate the deformation of next one year with every twelve alternative days and the predicted deformation values (mm) are presented in Table 3. As the analysis shows the subsidence in Nai dunia basti near Jharia (L4) is alarming as 93.8 mm /year where as Digwadih(L2) and Godhar(L5) showing critical rate as 82 mm/year during the period 2016–19. Based on the prediction result Godhar (L5) is showing alarming as 105 mm/year and L4 & L2 is showing 97 mm/year and 71 mm/year respectively.

## 5.3 Hyperparameters' influence

In this work, two hyperparameters are highly influenced on the accuracy and Time consumption which are (a) #of LSTM layers and (b) Size of the input. We conduct experiments on these hyperparameters and plot the results in Figs. 12 and 13.

In Fig. 12, we evaluate the accuracy by considering the two hyperparameters. In Fig. 12a, we assess the accuracy of fourteen data labels by increasing the # of LSTM layers in the stacked LSTM. We notice that increasing the number of layers also increases the accuracy. Similarly, we evaluate the accuracy by increasing the input data's size, and the results are plot in Fig. 12b. Here, we observe that increasing the input size also increases the accuracy. In Fig. 13, we evaluate the computation time per epoch by considering the two hyperparameters. In Fig. 13a, we assess the time computation of fourteen data labels by increasing the # of LSTM layers in the stacked LSTM. We notice that increasing the number of layers also increases the computation time slightly. We conclude that increasing the layers in the stacked LSTM also increases the computational time. Similarly, we evaluate the time computation by increasing the input data's size, and the results are plot in Fig. 13b. Here, we observe that increasing the input size also increases the computational time. In the proposed

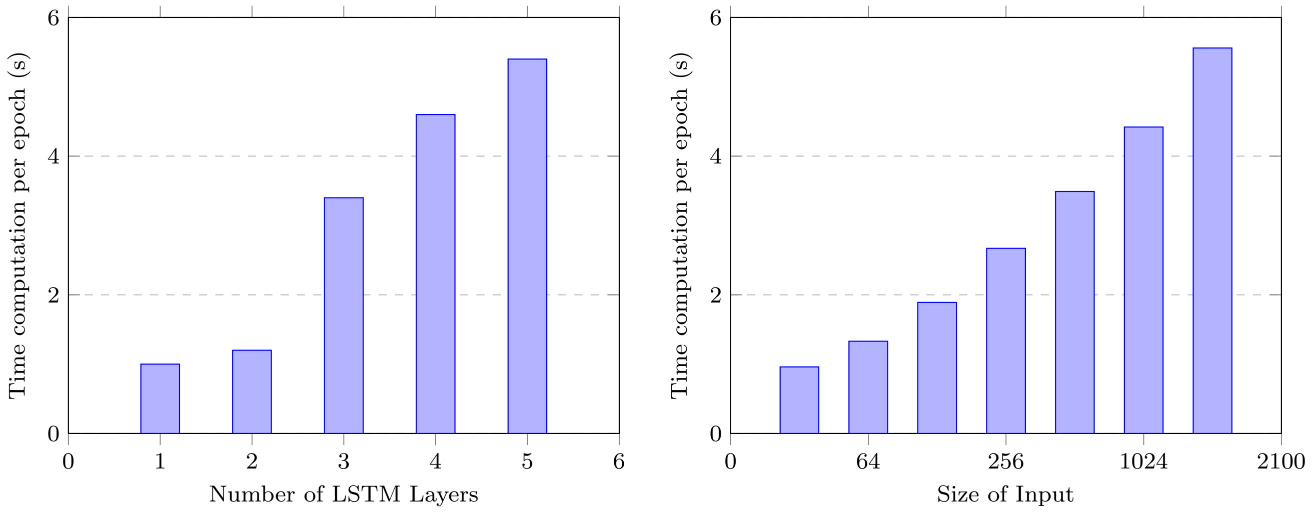

**(a)** **(b)**

**Fig. 13** Influence of Time computation with varying hyperparameters (**a**) #of LSTM Layers (**b**) Size of input

work, we used three layers to balance the prediction accuracy and computational time.

## 6 Conclusion

In this work, we have presented a new scientific approach for monitoring, validation and prediction of mining induced land subsidence in Jharia Coalfield using modified PSInSAR, GNSS and Recurrent Neural Networks. We have used the modified PSInSAR technique to collect the land subsidence value in an Excel sheet as well as colour coded pictorial views of the subsided locations. Some of PSs in the vicinity of GNSS survey points have been selected for prediction modelling. The cumulative displacement and deformation velocity during datasets period and during prediction period have been analysed and the suitable precaution mobel may be developed. We have used two variants of RNN are Vanilla LSTM and Stacked LSTM. We have collected 67 datasets pertaining to land subsidence at 14 various locations in JCF at an interval of 12 days. To perform prediction of land subsidence, we have trained, tested, and validated the predictive models by splitting datasets into 7:2:1. Finally, we have predicted the land subsidence for one year i.e, next 30 predictions in the interval of 12 days and demonstrated the prediction deformation values of all the 14 locations. All the predicted locations are finally validated with physical site visits accordingly. The prediction showed the subsidence rate in Nai-dunia basti in JCF is alarming as 93.8 mm /year whereas Digwadih and Godhar showed the critical rate as 82 mm/year.

**Acknowledgements** The authors would like to extends warm thanks to Dr. Daniele Perissin for providing access to SARPROZ software for this research study. The authors convey sincere thanks to the officials of the Department of Environment and Department of Surveying, BCCL, Dhanbad, India, for providing supports during the field studies.

## References

Abdikan S, Arıkan M, Sanli FB, Cakir Z (2014) Monitoring of coal mining subsidence in peri-urban area of zonguldak city (nw turkey) with persistent scatterer interferometry using alos-palsar. Environ Earth Sci 71(9):4081–4089

Abdikan S, Hooper A, Arikan M, Sanli FB, Cakir Z, Kemaldere H (2011) Insar time series analysis of coal mining in Zonguldak city, Northwestern Turkey

Amelung F, Jónsson S, Zebker H, Segall P (2000) Widespread uplift and ‘trapdoor’faulting on galapagos volcanoes observed with radar interferometry. Nature 407(6807):993–996

BCCL (2008) Master plan for dealing with fire, subsidence and rehabilitation in the leasehold of bccl

Chatterjee RS (2006) Coal fire mapping from satellite thermal ir data-a case example in Jharia coalfield, Jharkhand, India. ISPRS J Photogramm Remote Sens 60(2):113–128

Chatterjee RS, Fruneau B, Rudant JP, Roy PS, Frison P-L, Lakhera RC, Dadhwal VK, Saha R (2006) Subsidence of Kolkata (Calcutta) city, India during the 1990s as observed from space by differential synthetic aperture radar interferometry (d-insar) technique. Remote Sens Environ 102(1–2):176–185

Chatterjee RS, Thapa S, Singh KB, Varunakumar G, Raju EVR (2015) Detecting, mapping and monitoring of land subsidence in Jharia coalfield, Jharkhand, India by spaceborne differential interferometric SAR, GPS and precision levelling techniques. J Earth Syst Sci 124(6):1359–1376

Chatterjee RS, Singh KB, Thapa S, Kumar D (2016) The present status of subsiding land vulnerable to roof collapse in the Jharia coalfield, India, as obtained from shorter temporal baseline c-band dinsar by smaller spatial subset unwrapped phase profiling. Int J Remote Sens 37(1):176–190

Che Z, Purushotham S, Cho K, Sontag D, Liu Y (2018) Recurrent neural networks for multivariate time series with missing values. Sci Rep 8(1):1–12

Crosetto M, Crippa B, Biescas E, Monserrat O, Agudo M, Fernández P (2005) Land deformation measurement using sar interferometry: state-of-the-art. Photogrammetrie Fernerkundung Geoinf 2005(6):497

Crosetto M, Monserrat O, Cuevas-González M, Devanthéry N, Crippa B (2016) Persistent scatterer interferometry: a review. ISPRS J Photogramm Remote Sens 115:78–89

Dong S, Yin H, Yao S, Zhang F (2013) Detecting surface subsidence in coal mining area based on dinsar technique. J Earth Sci 24(3):449–456

Engelbrecht J, Inggs M (2013) Differential interferometry techniques on l-band data employed for the monitoring of surface subsidence due to mining. South African J Geom 2(2):82–93

Engelbrecht J, Inggs MR, Makusha G (2011) Detection and monitoring of surface subsidence associated with mining activities in the Witbank coalfields, South Africa, using differential radar interferometry. South African J Geol 114(1):77–94

Ferretti A, Prati C, Rocca F (2001) Permanent scatterers in sar interferometry. IEEE Trans Geosci Remote Sens 39(1):8–20

Gangopadhyay T, Tan SY, Huang G, Sarkar S (2018) Temporal attention and stacked lstms for multivariate time series prediction. In: NIPS 2018 workshop spatiotemporal blind submission

Guang L, Huadong G, Xiaofang G, Perski Z, Huanyin Y, et al. (2009) Mining area subsidence monitoring using multi-band sar data. In: 2009 Joint Urban remote sensing event, pp 1–6. IEEE

Gupta M, Mohanty KK, Kumar D, Banerjee R (2014) Monitoring surface elevation changes in Jharia coalfield, India using synthetic aperture radar interferometry. Environ Earth Sci 71(6):2875–2883

Hooper A (2008) A multi-temporal insar method incorporating both persistent scatterer and small baseline approaches. Geophys Res Lett. https://doi.org/10.1029/2008GL034654

Hooper A, Zebker HA (2007) Phase unwrapping in three dimensions with application to insar time series. JOSA A 24(9):2737–2747

Hooper A, Zebker H, Segall P, Kampes B (2004) A new method for measuring deformation on volcanoes and other natural terrains using insar persistent scatterers. Geophys Res Lett. https://doi.org/10.1029/2004GL021737

Hooper A, Bekaert D, Spaans K, Arıkan M (2012) Recent advances in sar interferometry time series analysis for measuring crustal deformation. Tectonophysics 514:1–13

Ishwar SG, Kumar D (2017) Application of Dinsar in mine surface subsidence monitoring and prediction. Curr Sci 112(1):46–51

Jianjun S, Chunjian H, Ping L, Junwei Z, Deyuan L, Minde J, Lin Z, Jingkai Z, Jianying S (2012) Quantitative prediction of mining subsidence and its impact on the environment. Int J Min Sci Technol 22(1):69–73

Jing-Xiang G, Hong H (2009) Advanced gnss technology of mining deformation monitoring. Proc Earth Planet Sci 1(1):1081–1088

Kumar S, Kumar D, Chaudhary SK, Singh N, Malik KK (2020) Land subsidence mapping and monitoring using modified persistent scatterer interferometric synthetic aperture radar in Jharia coalfield, India. J Earth Syst Sci 129(1):1–10

Lanari R, Lundgren P, Manzo M, Casu F (2004) Satellite radar interferometry time series analysis of surface deformation for Los Angeles, California. Geophys Res Lett. https://doi.org/10.1029/2004GL021294

Li H, Zhu L, Gong H, Sun H, Jie Y (2020) Land subsidence modelling using a long short-term memory algorithm based on time-series datasets. Proc Int Assoc Hydrol Sci 382:505–510

Liang S, Nguyen L, Jin F (2018) A multi-variable stacked long-short term memory network for wind speed forecasting. In: 2018 IEEE international conference on big data (Big Data). pp 4561–4564. IEEE

Lü W-C, Cheng S-G, Yang H-S, Liu D-P (2008) Application of GPS technology to build a mine-subsidence observation station. J China Univ Min Technol 18(3):377–380

Miao F, Yan M, Qi X, Ye C, Wang B, Liu R, Chen J (2008) Application of dinsar and gis for underground mine subsidence monitoring. Int Arch Photogramm Remote Sens Spat Inf Sci 37:251–255

Mora O, Mallorqui JJ, Broquetas A (2003) Linear and nonlinear terrain deformation maps from a reduced set of interferometric sar images. IEEE Trans Geosci Remote Sens 41(10):2243–2253

Mubashar M, Khan GM, Khan R (2021) Landslide prediction using long short term memory (LSTM) neural network on time series data in Pakistan. In: 2021 International conference on artificial intelligence (ICAI). pp 175–181. IEEE

Mura JC, Paradella WR, Gama FF, Silva GG, Galo M, Camargo PO, Silva AQ, Silva A (2016) Monitoring of non-linear ground movement in an open pit iron mine based on an integration of advanced dinsar techniques using terrasar-x data. Remote Sens 8(5):409

Pai S, Carr-Wilson S (2018) Total transition: the human side of the renewable energy revolution. Rocky Mountain Books Ltd

Pandey J, Kumar D, Singh VK, Mohalik NK (2016) Environmental and socio-economic impacts of fire in Jharia coalfield, Jharkhand, India: an appraisal. Curr Sci 110(9):1639–1650

Paradella WR, Ferretti A, Mura JC, Colombo D, Gama FF, Tamburini A, Santos AR, Novali F, Galo M, Camargo PO et al (2015) Mapping surface deformation in open pit iron mines of Carajás province (amazon region) using an integrated SAR analysis. Eng Geol 193:61–78

Perissin D, Wang T (2011) Repeat-pass sar interferometry with partially coherent targets. IEEE Trans Geosci Remote Sens 50(1):271–280

Prati C, Ferretti A, Perissin D (2010) Recent advances on surface ground deformation measurement by means of repeated space-borne sar observations. J Geodyn 49(3–4):161–170

Przyłucka M, Herrera G, Graniczny M, Colombo D, Béjar-Pizarro M (2015) Combination of conventional and advanced dinsar to monitor very fast mining subsidence with terrasar-x data: Bytom city (Poland). Remote Sens 7(5):5300–5328

Pu F, Xu Z, Chen H, Xu X, Chen N (2018) A dlm-lstm framework for north-south land deformation trend analysis from low-cost gps sensor time series. J Sens. https://doi.org/10.1155/2018/3054295

Qiao Y-L, Lai Y-K, Fu H, Gao L (2020) Synthesizing mesh deformation sequences with bidirectional LSTM. IEEE Trans Vis Comput Graph. https://doi.org/10.1109/TVCG.2020.3028961

Qin Y, Perissin D (2015) Monitoring underground mining subsidence in south indiana with c-and l-band insar technique. In: 2015 IEEE international geoscience and remote sensing symposium (IGARSS). pp 294–297. IEEE

Qu X, Yang J, Chang M (2019) A deep learning model for concrete dam deformation prediction based on RS-LSTM. J Sensors. https://doi.org/10.1155/2019/4581672

Rashid KM, Louis J (2019) Times-series data augmentation and deep learning for construction equipment activity recognition. Adv Eng Inf 42:100944

Raucoules D, Maisons C, Carnec C, Le Mouelic S, King C, Hosford S (2003) Monitoring of slow ground deformation by ers radar interferometry on the vauvert salt mine (France): Comparison with ground-based measurement. Remote Sens Environ 88(4):468–478

Schmidt DA, Bürgmann R (2003) Time-dependent land uplift and subsidence in the Santa Clara Valley, California, from a large interferometric synthetic aperture radar data set. J Geophys Res Solid Earth. https://doi.org/10.1029/2002JB002267

Sefercik UG, Soergel U (2014) Influence of temporal baseline on the vertical absolute accuracies of tsx hs interferometric dsms: Case study on berlin. Int Arch Photogramm Remote Sens Spatial Inf Sci

Shen S-L, Njock PGA, Zhou A, Lyu H-M (2021) Dynamic prediction of jet grouted column diameter in soft soil using Bi-LSTM deep learning. Acta Geotech 16(1):303–315

Strozzi T, Wegmuller U, Tosi L, Bitelli G, Spreckels V (2001) Land subsidence monitoring with differential sar interferometry. Photogramm Eng Remote Sens 67(11):1261–1270

Suchowerska Iwanec AM, Carter JP, Hambleton JP (2016) Geomechanics of subsidence above single and multi-seam coal mining. J Rock Mech Geotech Eng 8(3):304–313

Thapa S, Chatterjee RS, Singh KB, Kumar D (2016) Land subsidence monitoring using ps-insar technique for l-band sar data. Int Arch Photogramm Remote Sens Spatial Inf Sci 40:2016

The SAR PROcessing tool by periZ. http://www.sarproz.com, 2019. Accessed: 2021/11/12 15:35:45

Trivedi (2020) Land subsidence threat by 2026

Wang J, Peng X, Xu CH (2011) Coal mining GPS subsidence monitoring technology and its application. Min Sci Technol 21(4):463–467

Wei CC (2020) Development of stacked long short-term memory neural networks with numerical solutions for wind velocity predictions. Adv Meteorol 2020

Yue H, Liu G, Perski Z, Guo H (2011) Satellite radar reveals land subsidence over coal mines. SPIE Newsroom. 3

Zhou C, Gong H, Chen B, Li J, Gao M, Zhu F, Chen W, Liang Y (2017) Insar time-series analysis of land subsidence under different land use types in the eastern Beijing plain, China. Remote Sens 9(4):380